Particles II

Access the latest eBook →

11 Advanced Optical Metrology

Particles II

EVIDENT OLYMPUS

WILEY

Impact on Biological Systems and the Environment

This eBook is dedicated to the research of Professor David Wertheim.
In collaboration with various groups, Professor Wertheim uses confocal microscopy to analyse the impact of different types of particles on human health and the environment, with a focus on human health-hazardous particles detected with solid-state nuclear track detectors (SSNTD). Download for free, today.

EVIDENT OLYMPUS

WILEY

Top-Layer Engineering Reshapes Charge Transfer at Polar Oxide Interfaces

Gabriele De Luca*, Jonathan Spring, Moloud Kaviani, Simon Jöhr, Marco Campanini, Anna Zakharova, Charles Guillemard, Javier Herrero-Martin, Rolf Erni, Cinthia Piamonteze, Marta D. Rossell, Ulrich Aschauer, Marta Gibert*

G. De Luca, J. Spring, S. Jöhr, M. Gibert

Department of Physics, University of Zurich, Winterthurerstrasse 190, 8057 Zurich, Switzerland. E-mail: gabriele.deluca@icn2.cat, gibert@ifp.tuwien.ac.at

M. Kaviani, U. Aschauer

Department of Chemistry, Biochemistry and Pharmaceutical Sciences, University of Bern, Freiestrasse 3, 3012 Bern, Switzerland.

M. Campanini, R. Erni, M. D. Rossell

Electron Microscopy Center, Empa, Swiss Federal Laboratories for Materials Science and Technology, Überlandstrasse 129, 8600 Dübendorf, Switzerland.

A. Zakharova, C. Piamonteze

Swiss Light Source, Paul Scherrer Institut, 5232 Villigen PSI, Switzerland.

C. Guillemard, J. Herrero-Martin

ALBA Synchrotron Light Source, 08290 Cerdanyola del Vallès, Barcelona, Spain.

G. De Luca

Current address: Catalan Institute of Nanoscience and Nanotechnology (ICN2), Campus UAB, 08193 Bellaterra, Barcelona, Spain.

M. Gibert

Current address: Institute of Solid State Physics, TU Wien, Wiedner Hauptstrasse 8-10, 1040 Wien, Austria

Charge-transfer phenomena at heterointerfaces are a promising pathway to engineer functionalities absent in the bulk material but can also lead to degraded properties in the ultrathin films. Mitigating such undesired effects with an interlayer reshapes the interface architecture, restricting its operability. Therefore, developing less-invasive methods to control the charge transfer would be beneficial. Here, an appropriate top-interface design allows for remotely manipulating the charge configuration of the buried interface and concurrently restoring the ferromagnetic trait of the whole film. Double-perovskite insulating ferromagnetic La_2NiMnO_6 (LNMO) thin films grown on perovskite oxide substrates are investigated as a model system. An oxygen-vacancy-assisted electronic reconstruction takes place initially at the LNMO polar interfaces. As a result, the magnetic properties of 2-5 unit cells LNMO films are affected beyond dimensionality effects. The introduction of a top electron-acceptor layer redistributes the electron excess and restores the ferromagnetic properties of the ultrathin LNMO films. Such a strategy can be extended to other interfaces and provides an advanced approach to fine tune the electronic features of complex multi-layered heterostructures.

1. Introduction

In the last two decades, a growing interest in charge-transfer phenomena in oxide heterostructures resulted in the discovery of many interfacial properties that are not exhibited by the bulk counterparts. The most famous example concerns the emergence of a two-dimensional electron liquid at the interface between $LaAlO_3$ (LAO) and $SrTiO_3$ (STO),[1] but other investigations involving transition metal cations with partially filled *d*-bands revealed that interfacial ferromagnetism,[2] exchange bias,[3] and orbital reconstructions[4,5] can be targeted with proper material design.[6]

Interfacial charge-transfer phenomena, however, are also associated with detrimental effects on the desired functionalities, especially in the ultrathin limit.[7,8] A favorable strategy to control the extent of charge transfer consists in inserting a specific interlayer that modulates the electrostatic screening at the interface.[9] Unfortunately, this approach cannot be used if one would like to retain certain properties of the original interface (for instance, octahedral connectivity[10,11] or substrate-driven field effect[12,13]). Therefore, alternative methods to influence the electronic configuration of a buried oxide interface are very intriguing.[14,15]

In this work we demonstrate that the heterointerface between a polar ferromagnetic insulating double perovskite thin film (La_2NiMnO_6, LNMO) and a non-polar single perovskite substrate (STO) is a prototypical example of an interfacial charge transfer triggered by a polarity mismatch.[16] The resulting electronic reconstructions strongly affect the magnetic properties of the heterostructure, adding to dimensionality effects. To restore the optimal electronic configuration of the buried interface, we design a top-interface engineering approach through a $LaNiO_3$ (LNO) overlayer. The presence of LNO is fundamental in displacing the interfacial charge and allows reestablishing the ferromagnetism in LNMO. This method can be extended to other systems and certifies that top-

3

interface engineering can be successfully exploited to remotely control the electronic configuration of buried complex oxide interfaces.

2. Results and discussion

2.1 Magnetic properties of LNMO//STO heterostructures

LNMO is a ferromagnetic insulator with a bulk Curie temperature (T_C) around 270 K, resulting from strong positive superexchange between the long-range-ordered Ni^{2+} ($3d^8$) and Mn^{4+} ($3d^3$) cations in a rock-salt-type structure.[17–19] To evaluate dimensionality and interface effects on LNMO magnetic and electronic properties, we grew a set of films of different thicknesses, ranging from 90 to 2 pseudocubic unit cells (pc uc), on prototypical STO substrates (tensile strain = +0.7%). Structural characterization indicates epitaxial growth and high crystalline and surface quality in all the films (**Figure S1**).[19] As shown in **Figure 1a**, films thicker than 30 uc (~ 12 nm) exhibit bulk-like ferromagnetic properties, i.e. T_C ~ 270 K and saturation magnetization larger than 4 μ_B/formula units.[19] However, the Curie temperature and the magnetization decrease as films are grown thinner. Still, 15- and 5-uc-thick films display T_C ~ 250 K and T_C ~ 165 K, respectively.
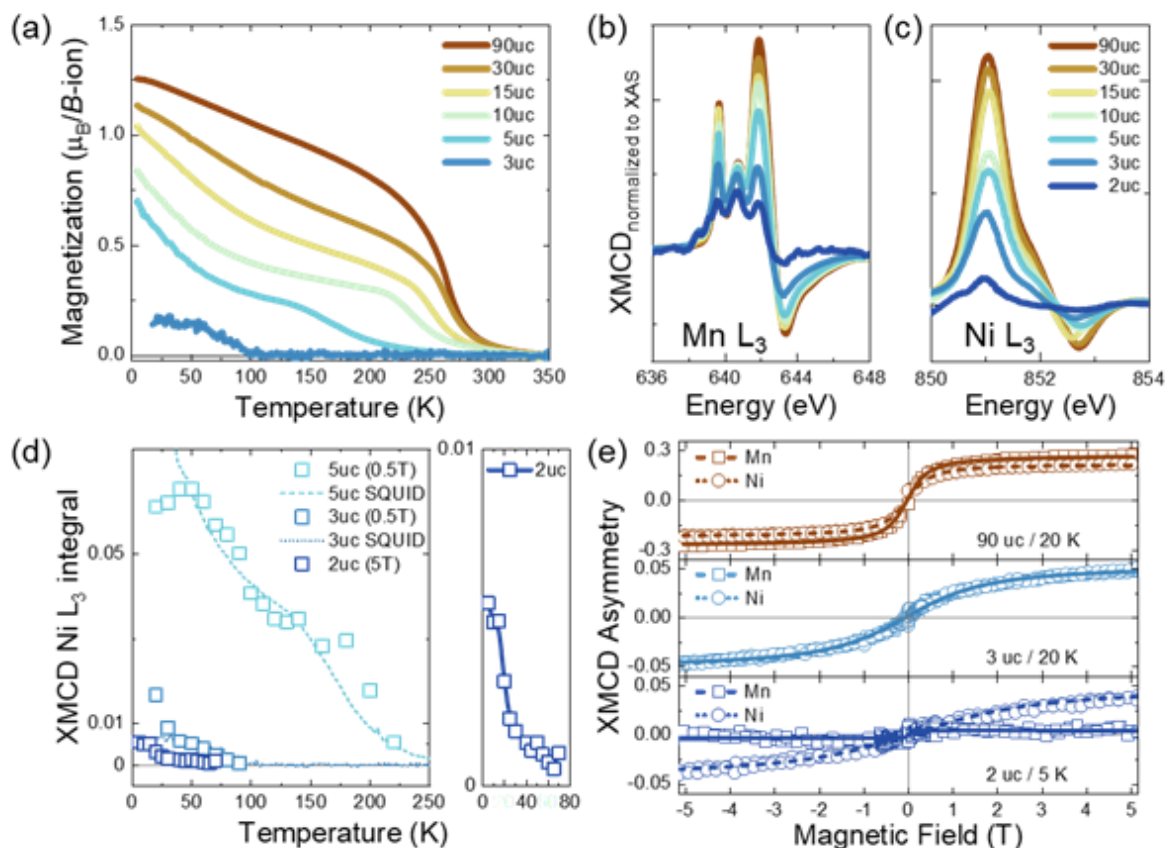
Figure 1. a) Magnetization vs temperature measured in a magnetic field of 0.5 T for various LNMO film thicknesses. b) Mn L_3-edges XMCD spectra measured at 20 K and 5 T. c) Same as b) for Ni. d) Integral of the Ni XMCD L_3-edge as a function of the sample temperature for selected film thicknesses. Scaled data from SQUID is shown for comparison (dashed and dotted lines). In the right panel, the behavior of the ultrathin 2 uc film is highlighted. Here, the line is a guide to the eye. e) XMCD asymmetry as a function of the magnetic field calculated at both Mn and Ni L_3-edges for the 90 uc (top panel, 20 K), 3 uc (middle panel, 20 K) and 2 uc (bottom panel, 5 K) LNMO films. The lines are guides to the eye.

This magnetic trend is further confirmed by x-ray magnetic circular dichroism (XMCD) measurements. The reduction of both Mn and Ni $L_{3,2}$ integrals in normalized XMCD spectra is indicative of a decrease in the magnetic moment of both the Mn and Ni sublattices in the ultrathin

limit (L$_3$-edges shown in **Figure 1b-c**, the full L$_{3,2}$-edges displayed in **Figure S2**). In **Figure 1d**, we plot the evolution of the Ni XMCD L$_3$-integral as a function of the temperature as an alternative way to determine the Curie temperature. The elemental sensitivity of XMCD compared to SQUID magnetometry allows films as thin as 2 uc (~ 0.8 nm) to be characterized. We find that 2 uc films have T$_C$ ~ 10 K.

To gain insight into the origin of this thickness-dependent degradation of the magnetic properties, it is instructive to observe the difference between the Mn and Ni XMCD asymmetry measured as a function of the external magnetic field for different film thicknesses, as displayed in **Figure 1e**. For a bulk-like 90-uc-thick film, both the Mn and Ni asymmetry saturate at similar values of the magnetic field. For a 3-uc-thick film we still observe a similar behavior between Mn and Ni despite asymmetries saturating at larger fields. For the 2-uc-thick film, the Ni sublattice behavior is still reminiscent of a ferromagnetic hysteresis whereas the Mn sublattice is severely affected by the thickness reduction, nearly losing its ferromagnetic character.

2.2 Charge transfer induced by interfacial polarity mismatch

Since the electronic configuration of Ni and Mn is key to the ferromagnetic behavior of the LNMO system,[17] we investigated the valence state of the cations using x-ray absorption spectroscopy (XAS). In **Figure 2a**, we show the L$_{3,2}$-edges of Mn as a function of the LNMO thickness. The XAS data of the 90 uc sample is consistent with previous observations on bulk specimens and certifies the valence state of Mn to be prevalently 4+.[20] As the film thickness is reduced, a pronounced shoulder in the low-energy range and an increased spectral weight around 641 eV emerge. These can be

associated with an increase of Mn^{3+} content located at the interface between LNMO and STO. However, we cannot exclude the presence of additional Mn^{3+} states present also in the top surface layer, as we previously detected in 30-uc-thick LNMO//STO heterostructures.[19] We also observe a small alteration of the Ni valence state (**Figure 2b**) to which we will come back.

From previous structural characterizations, we know that our relatively-thick LNMO films grow with a prevalent rock-salt ordering of Ni^{2+} and Mn^{4+} cations and display bulk-like T_C and saturation magnetization.[19] Therefore, we can exclude sub-optimal growth conditions. It is known that in perovskite oxide films the formation energy of bulk oxygen vacancies is reduced with increasing tensile strain.[21] A systematic XAS study on 5-uc-thick LNMO films grown on a variety of substrates (imposing epitaxial strains ranging from -2.1% to +1.8%[19]) reveals that the LNMO film with the largest Mn^{3+} content is the one grown on STO, followed by the one grown on LSAT (**Figure S3**). As none of these two substrates exerts the largest tensile strain on the films, the strain-triggered oxygen-vacancy-formation scenario cannot be the dominant mechanism involved.
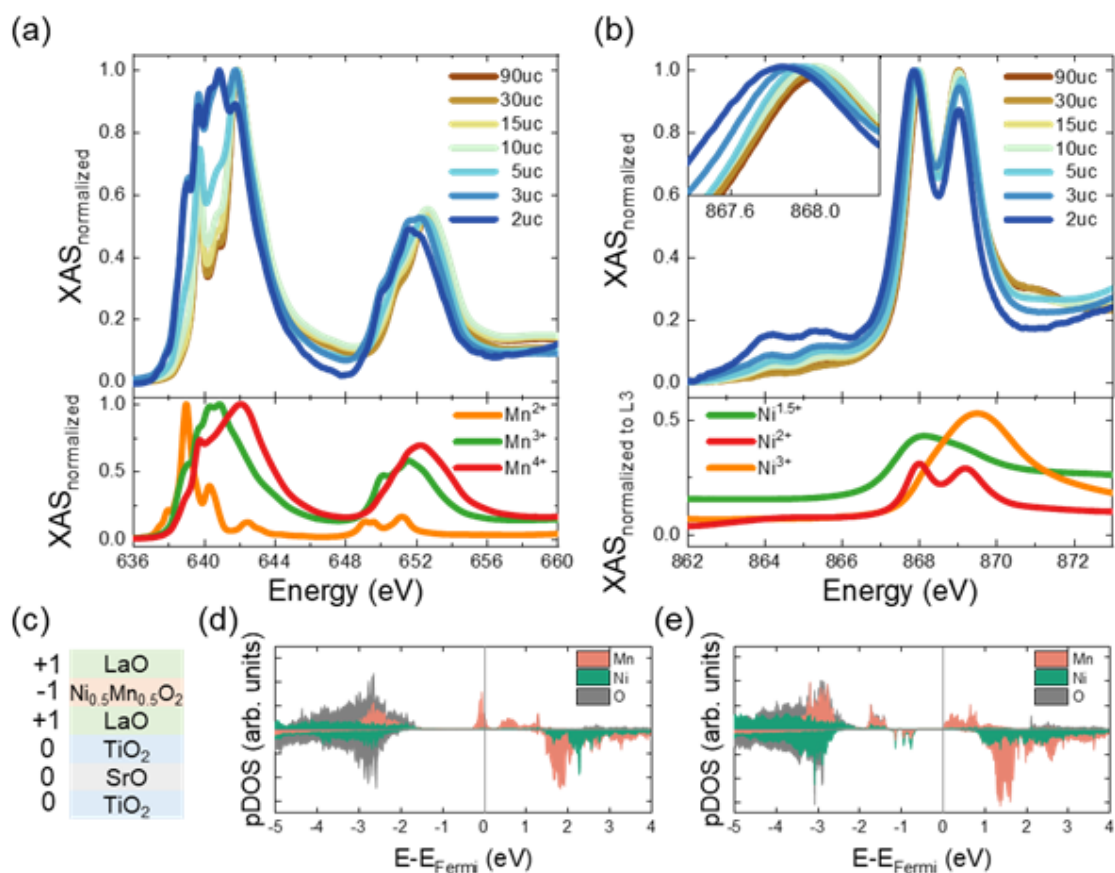
Figure 2. a) XAS of Mn $L_{3,2}$-edges for different LNMO thicknesses (top panel). Data is collected at 20 K. Reference XAS spectra for various electronic configurations of Mn[22] (bottom panel). b) Same as a) for Ni L_2-edge[23]. The Ni L_3-edge overlaps with the La M_4-edge and it is not shown. In inset, a zoom on the Ni L_2-edge maxima highlights the progressive shift to lower energies for decreasing LNMO thickness. c) Sketch of interfacial stacking sequence of LNMO//STO. The nominal ionic charge of each layer is indicated on the left. d) pDOS for the $Ni_{0.5}Mn_{0.5}O_2$ layer adjacent to the LNMO//STO interface. Mn states at the Fermi level indicate the presence of charge transfer. e) pDOS for the interfacial $Ni_{0.5}Mn_{0.5}O_2$ layer in presence of oxygen vacancies. In this case both majority spin Mn and minority spin Ni states are populated by the excess electrons. The overlap between Mn and Ni states is due to orbital hybridization.

Instead, we should recall that the ABO_3 perovskite crystal structure can be thought of as a sequence

of AO and BO_2 planes that carry a nominal ionic charge depending on the specific A and B cations.

This applies to the LNMO//STO interface which can be pictured as a sequence of uncharged $(SrO)^0$

and $(TiO_2)^0$ layers followed by charged $(LaO)^+$ and $(Ni_{0.5}Mn_{0.5}O_2)^-$ stacks along the $[001]_{pc}$ orientation (**Figure 2c**). Hence, the polar discontinuity at the interface builds up a diverging potential, generally referred to as "polar catastrophe" that can be relieved by an electronic reconstruction.[16]

To investigate the implications of this, we performed density functional theory (DFT) calculations. Layer-resolved projected density of states (pDOS) for the stoichiometric LNMO//STO heterostructure without oxygen vacancies reveals the appearance of Mn electronic states located at the Fermi level in the $Ni_{0.5}Mn_{0.5}O_2$ layer adjacent to the TiO_2-interface layer as a mechanism to counteract the polar discontinuity (**Figure 2d**). Interestingly, this electron redistribution is not accompanied by a concomitant change in the Ni electronic states. Equivalent calculations for an LNMO//LaGaO$_3$ (LGO) heterostructure, which is characterized by a similar tensile strain (= +0.4%) but without polar discontinuity, show no trace of extra states (**Figure S4**). These results support the emergence of an electronic reconstruction at the LNMO//STO interface with the interfacial electrons preferentially localized at the Mn sites, similar to what already observed in LaMnO$_3$//STO.[24,25]

From the DFT calculations, the built-in electric field within the LNMO film is estimated to be about 0.118 V Å^{-1}. Using the computed LNMO bandgap (~ 1.66 eV) to estimate the critical LNMO thickness for the polar-discontinuity-induced electronic reconstruction, we obtain ~ 3.65 uc (~ 14 Å). Experimentally, however, we observe an electron redistribution in films as thin as 2 uc (Figure 2a-b), suggesting that the ionic picture alone is not sufficient to explain the electronic configuration of our ultrathin LNMO films. It has been argued that a discontinuity in the interface polarity can also be a driving force for the formation of oxygen vacancies.[26,27] Note that the origin of these interfacial oxygen vacancies is not epitaxial strain[21] but rather the polar discontinuity itself.

To contemplate this possibility, we performed additional DFT calculations introducing oxygen vacancies in our heterostructure (**Figure S5**). We find it is most favorable for the system to form oxygen vacancies when these are located at the film surface, followed by positions in the $Ni_{0.5}Mn_{0.5}O_2$ interfacial slab. Breaking substrate Ti-O bonds, instead, leads to higher formation energies. In this scenario, due to extra electron doping from the oxygen vacancies and a defect-state-induced band gap reduction, an LNMO thickness smaller than 3.65 uc is enough to trigger the electronic reconstruction, in line with our XAS observations. These calculations further reveal that a few of the oxygen-vacancies-induced doping electrons are now also populating the minority spin Ni states in the $Ni_{0.5}Mn_{0.5}O_2$ layer adjacent to the substrate, besides Mn (**Figure 2e** and Figure S5b). This indicates the appearance of $Ni^{(2-x)+}$ states at the LNMO//STO interface modelled with oxygen vacancies, in contrast with the simple ionic picture calculations previously discussed.

Experimentally, when decreasing the LNMO thickness on STO substrates, we observe a shift to lower energies of the Ni L_2-edge spectral weight (Figure 2b) suggesting a small reduction of the Ni valence state at the LNMO interfacial layers. Thus, both the calculations and the experimental observations indicate that a complex polarity-induced charge transfer mediated by oxygen vacancies is taking place within the LNMO films to compensate their polar discontinuity with the substrate. This scenario intuitively explains the presence of Mn^{3+} also observed at the (less) polar LNMO//LSAT interface.[19,28] Notice that all other perovskite substrates constitute nonpolar interfaces with LNMO and therefore in these heterostructures we always observe a reduced amount of Mn^{3+} compared to the STO and LSAT ones (Figure S3).

2.3 Atomically resolved cation and electron distribution

To further verify our observations, we performed energy dispersive x-ray (EDX) and electron energy-loss spectroscopy (EELS) analyses across the LNMO//STO heterostructures in a scanning transmission electron microscope (STEM). By imaging the films along the $[110]_{pc}^{LNMO}$ zone axis we get insight into the Ni-Mn cationic order.[19,29] The high-angle annular dark-field (HAADF) STEM image of a representative 13 uc LNMO//STO film is presented in **Figure 3a** together with the combined EDX elemental maps obtained for Mn, Ni and Ti (**Figure 3b**). The individual elemental maps are shown in **Figure S6**. We observe epitaxial coherent growth with absence of defects such as dislocations or precipitates through the entire surveyed area. From the EDX map, we deduce that the first layer is partially intermixed with Ti, as often realized at the interface between a polar transition metal oxide and STO.[30,31] Note that this tendency of the transition metal cation and Ti to swap is generally not enough to screen the interfacial polarity.[32] Away from the interface, we see that the film grows in a perfectly-ordered manner,[19] as evidenced by the checkerboard patterns observed in the EDX maps. Closer to the interface, we can appreciate the existence of a transition region of around 5-6 uc with only partial rock-salt ordering of the LNMO film. DFT calculations considering various NiO_6 and MnO_6 octahedra double-perovskite configurations, namely rock salt, layered and columnar, show that rock-salt ordering is the most stable configuration for LNMO. However, the presence of an additional electron, such as the one transferred to the interface due to the polar discontinuity, turns the columnar ordering into the most favorable structure (**Figure S7**). Hence, in the proximity of the Mn^{3+} ions located at the LNMO//STO heterointerface an increased tendency to B/B'-site disorder is expected, in agreement with the EDX elemental maps shown in Figure 3b and Figure S6.
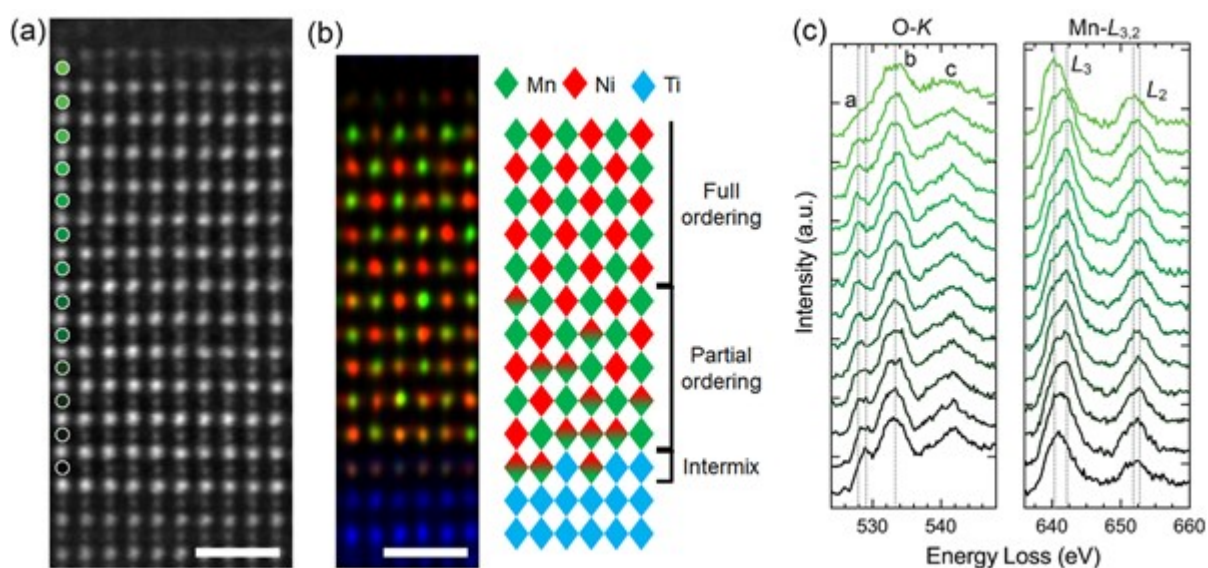
Figure 3. a) HAADF image of a 13 uc LNMO//STO film. b) STEM-EDX map showing the distribution of Mn (green), Ni (red) and Ti (blue) in the LNMO//STO heterostructure, and schematic of the cation distribution in the octahedral sites. c) EELS of the O K and Mn $L_{3,2}$ edges across the LNMO//STO heterostructure obtained at the positions indicated by the colored dots in panel a). The intensity was normalized to the O K_b main peak and the Mn L_3 line. The scale bars are 1 nm.

Further, our STEM-EELS data confirm the formation of oxygen vacancies both in the $Ni_{0.5}Mn_{0.5}O_2$ interfacial layers and at the film surface. In **Figure 3c**, we show the O K and Mn $L_{3,2}$ edges acquired across the LNMO film thickness at the layer positions indicated with colored dots in Figure 3a. The EEL spectra acquired at the middle $Ni_{0.5}Mn_{0.5}O_2$ layers (layers 3 to 12 from the interface) certify the valence state of Mn to be prevalently 4+. However, at the $Ni_{0.5}Mn_{0.5}O_2$ interfacial layers, the Mn L_3 edge shifts to lower energies (from ~ 642 to ~ 641 eV) and the O K_a pre-edge peak shifts to higher energies (from ~ 528 to ~ 529 eV). An even larger shift of the Mn L_3 edge of ~ 2 eV is observed at the

film surface, while the O K$_a$ pre-edge peak almost disappears. These observations are associated with an increase of Mn^{3+} content and oxygen vacancies located at the LNMO//STO interface and at the LNMO film surface,[33,34] which is in excellent agreement with the DFT calculations. We can also use the EELS data to quantify the local Mn valence state of each Mn$_{0.5}$Ni$_{0.5}$O$_2$ layer. The obtained results are shown as vertical dashed lines in the right panel of **Figure S6b**. Using the procedure described in the methods section, we obtain an average valence state of the interfacial manganese atoms of +3.4, while a value of +3.1 is retrieved for the surface manganese atoms. At the interface, the fractional contributions of Mn^{3+} and Mn^{4+} are determined as 0.6 and 0.4, respectively.

2.4 Charge-transfer engineering via top-interface design

The electronic configuration obtained from both experimental and theoretical investigations of the LNMO//STO heterostructure is depicted in **Figure 4a**. Electron-doped states triggered by the polar-discontinuity-induced oxygen vacancies are present at both interfaces. As these states are detrimental for the Mn^{4+}-Ni^{2+}-related LNMO ferromagnetism,[17,35] we want to control their extent. To this aim, we capped the LNMO layers with LaNiO$_3$ (LNO). This compound is characterized by bulk paramagnetic metallic behavior over the whole temperature range[36] and its Ni^{3+} cation is a well-known electron-acceptor.[2,3,5,37,38] Due to the strong electronegativity difference between Mn^{3+} and Ni^{3+},[17,38] in the LNO/LNMO//STO heterostructure, the effects of the polar discontinuity present at the LNMO *bottom* interface can potentially be relieved by an electronic reconstruction taking place at the LNMO *top* interface, towards the LNO side (**Figure 4b**). We verified the feasibility of this

scenario by aligning the DFT density of states of LNMO and LNO via their work functions, as detailed in **Figure S8**.
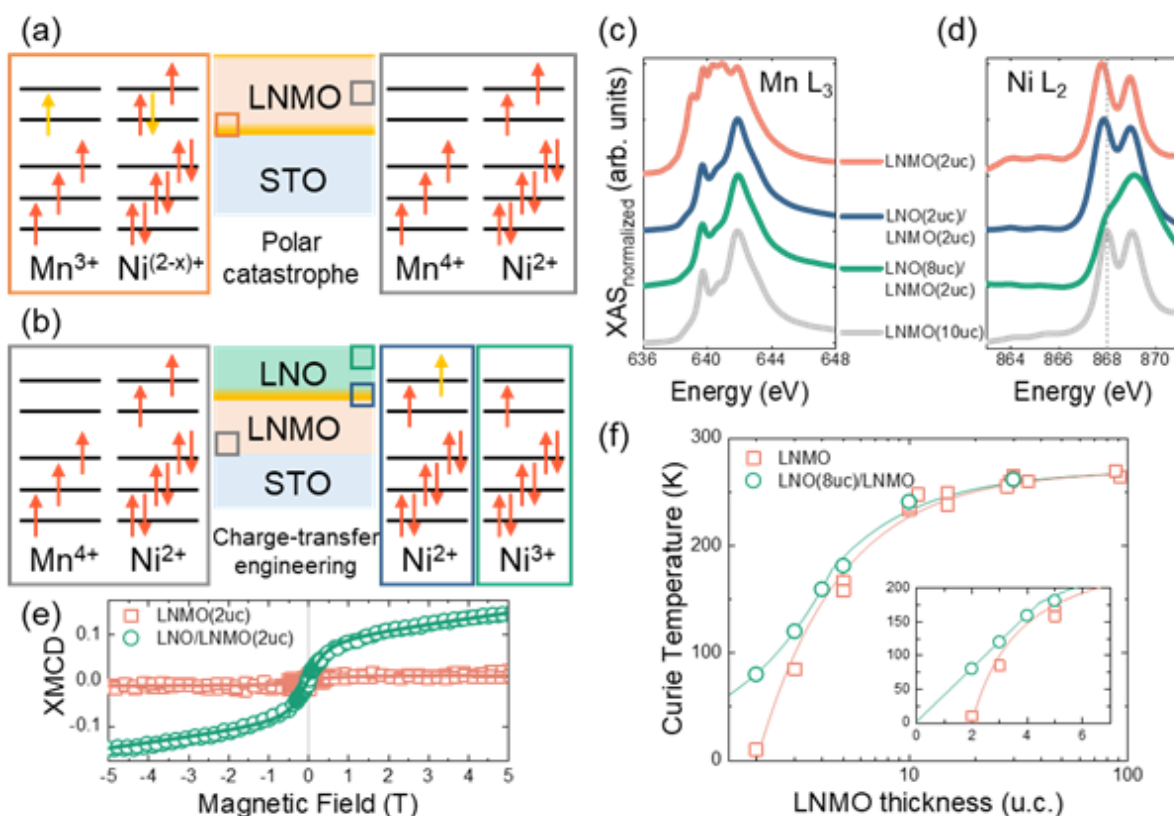

Figure 4. a) Schematic of the charge configuration of the LNMO//STO heterostructure in presence of oxygen vacancies. Electrons transferred to the interfaces are depicted in yellow. b) New charge configuration after capping the LNMO//STO heterostructure with LNO. The doping electrons are now populating the first few LNO layers. In both a) and b), the colored squares highlight the location within the heterostructures of the indicated electronic configuration. c) XAS at Mn L_3 edge of a 2-uc-thick LNMO film with and without top LNO. 10-uc-thick LNMO shown for comparison. Spectra shifted for better visibility. d) Same as c) for the Ni L_2 edge. The dashed line indicates the energy of the Ni L_2-edge maximum of the reference LNMO sample. e) Mn XMCD asymmetry measured at 20 K for LNO/LNMO//STO (green circles) and LNMO//STO (red squares) heterostructures. Lines are a guide to the eye. f) Measured Curie temperature as a function of the LNMO thickness (log scale) for engineered (green circles) and bare (red squares) heterostructures. The data are fitted using a linear function and a power law for the capped heterostructures and a power law for the uncapped heterostructures.[39] The inset shows the low-thickness range using a linear scale.

14

The striking effect of LNO on the Mn/Ni electronic configuration of our LNMO//STO heterointerfaces is observed in the Mn and Ni $L_{3,2}$-edge XAS spectra (**Figure 4c-d**). The Mn^{3+} content present in a bare electron-doped 2-uc-thick LNMO is markedly reduced upon capping it with a 2-uc-thick LNO overlayer. The same effect is also obtained on a 5-uc-thick LNMO film (**Figure S9a**). Such a drastic change in the Mn electronic configuration is not observed instead when the LNMO films are capped with LAO, as shown in Figure S9a and as predicted by our DFT calculations (Figure S8). We can therefore exclude that in our LNO/LNMO//STO heterostructure, La vacancies (instead of Ni) are playing the role of electron acceptors.[40] Indeed, when the LNO overlayer is only 2 uc thick, the overall Ni L_2-edge shape suggests that the Ni in LNO adopts a 2+ configuration (blue square and blue line in Figure 4b and 4d, respectively). A transition to more conventional Ni^{3+} (green square in Figure 4b) is observed instead when the LNO thickness is increased (i.e., the case of 8 uc LNO capping shown by the green line in Figure 4d). The fact that the charge transfer is not observed when LAO is used as capping layer (the Al cation has no *d* electrons) highlights the pivotal role of Ni^{3+} in engineering such a functionality. We also verified the generality of this approach by characterizing LNO/LNMO//LSAT heterostructures with XAS (**Figure S9b**). The observation of the same functional behavior on another polar interface further corroborates the ability of LNO to attract the electrons that are doping the opposite interface due to a polar discontinuity between the film and the substrate.

As a result of this optimized electronic configuration, the magnetic properties of the LNO/LNMO//STO heterostructures are drastically enhanced. As shown in **Figure 4e** through the field-dependence of the Mn XMCD asymmetry measured at 20 K, the ferromagnetic behavior of the

Mn sublattice in a 2-uc-thick LNMO film is recovered upon LNO capping. The remarkable thickness-dependent evolution of the Curie temperature is summarized in **Figure 4f**. We observe a systematic boost of T_C in the top-interface-engineered heterostructures that are 5-uc-thick or less. For example, a LNO-capped 2(5)-uc-thick LNMO is characterized by a T_C ~ 80 (180) K as determined by combined XMCD and SQUID magnetometry (**Figure S10**). This is to be compared with T_C ~ 10 (165) K for a bare 2(5)-uc-thick LNMO film (Figure 1d). For thicker LNMO films, the improvement is less evident given the reduced fraction that the interfacial layers contribute to the total film thickness and due to the increased distance between top and bottom interface that can inhibit the interlayer charge transfer.[41]

Furthermore, it should be noted that in the bare LNMO//STO heterostructures, a conventional power law reduction of T_C is observed in the whole thickness range. For the LNO-engineered heterostructures, we can rather appreciate the presence of two different regimes for T_C as a function of the LNMO thickness. The power law reduction at larger thickness is followed by a linear behavior in the ultrathin domain (inset of Figure 4f). This linear behavior is caused by the renormalization of the long-range spin-spin interaction due to finite size effects.[39] By extrapolating the linear behavior to 0 uc LNMO, we obtain a T_C value compatible with 0 K suggesting that the reduced dimensionality of the LNMO films is the only dominant factor determining the reduction of T_C in the interface-engineered LNO/LNMO//STO heterostructures.

3. Conclusion

We have shown that ultrathin LNMO//STO heterostructures experience a degradation of their magnetic properties and poorer Ni/Mn cation ordering as a consequence of an oxygen-vacancy-assisted electronic reconstruction taking place at LNMO polar interfaces. Introducing an LNO overlayer in these heterostructures redistributes the electron excess and restores the LNMO ferromagnetic properties. The LNO-induced electron migration is very general and can be adapted to other functional interfaces, being also obtained on heterostructures grown on LSAT, where a polarity mismatch takes place too. Such a top-interface engineering approach to manipulate the electronic state of a buried interface gets us closer to reaching a systematic and exact control of the desired functionalities in complex oxide heterostructures.

4. Methods

Sample preparation and characterization: LNO/LNMO//STO heterostructures were grown using off-axis radio-frequency magnetron sputtering in a flowing gas mixture of argon and oxygen stabilizing a pressure of 0.18 mbar. LNMO was grown at 720 °C while LNO was grown at 510 °C. The same conditions were used also on different substrates.[19] After the deposition, the heterostructures were cooled to room temperature in the same gas environment. Film thickness was calibrated via x-ray diffraction finite-size fringes[42] measured with a Rigaku Smartlab diffractometer operating in line focus mode with a monochromated Cu $K_{\alpha 1}$ radiation. Magnetic measurements were carried out in a Quantum Design superconducting quantum interference device (SQUID) magnetometer operating in vibrating sample mode (VSM) with the magnetic field applied parallel to the plane of the sample. A residual magnetic moment from the STO substrates has been subtracted. Curie temperatures were

determined from SQUID magnetometry taking the minimum of the derivative of the magnetic moment.

X-ray absorption spectroscopy (XAS) and x-ray magnetic circular dichroism (XMCD): Measurements were performed at both the X-Treme beamline[43] at the Swiss Light Source (SLS) and BOREAS beamline[44] at the ALBA Synchrotron. The spectra were acquired by measuring the total electron yield (TEY) with an incidence angle (the angle between the x-ray beam direction and the sample normal) of 60°. The XAS curves are obtained as the sum of spectra measured with vertical and horizontal linear polarization and are normalized to the peak of the respective $L_{3,2}$-edge. The reference spectra are obtained from $MnCl_2$ (Mn^{2+}), Mn_2O_3 (Mn^{3+}), $SrMnO_3$ (Mn^{4+}), $Nd_{0.8}Sr_{0.2}NiO_{2+\delta}$ ($Ni^{1.5+}$), NiO (Ni^{2+}), and $NdNiO_3$ (Ni^{3+}) and are normalized to the peak of the respective L_3-edge. The $Nd_{0.8}Sr_{0.2}NiO_{2+\delta}$ sample is obtained using a topotactic reduction.[45] Only for this specific case, the effective Ni valence is inferred by comparison with charge transfer multiplet theory calculations.[46] The XMCD is defined as the difference between spectra measured with left and right circular polarization and normalized to the L_3 maximum from the XAS. The XMCD asymmetry is defined as $\frac{L-R}{L+R}$ with L (R) obtained as the difference between the L_3-resonant and off-resonant energies for left (right) circular polarization.[19] The XMCD Ni L_3 integral values as a function of the temperature presented in Figure 1d have been obtained in an external magnetic field of 0.5 T for the 5- and 3-uc-thick LNMO films, and in an external magnetic field of 5 T for the 2-uc-thick film. This difference in magnetic field intensity causes an increase in T_C of around 10 K.[19] This information has been used for a more realistic determination of T_C in the thinner LNMO sample.

Density functional theory (DFT) calculations: DFT calculations were performed using the PBEsol exchange-correlation functional as implemented in the VASP package.[47] Electron-core interactions were described via the projector augmented wave (PAW) method[48] with La(5s,5p,5d,6s), Mn(3p,3d,4s), Ni(3p,3d,4s), Sr(4s,4p,5s), Ti(3s,3p,3d,4s) and Ga(3d,4s,4p). Valence shells and wave functions were expanded in a plane waves basis with 500 eV kinetic energy cutoff. A Hubbard U correction[49] was applied to the d states of Mn (3.0 eV), Ni (6.0 eV) and Ti (4.0 eV). The interface was modeled as cell with $\sqrt{2} \times \sqrt{2}$ in-plane dimension (5.454×5.454 Å) with respect to the 5-atom cubic cell. In the out-of-plane direction, 4 uc layers of STO and 6 uc layers of LNMO were used together with a vacuum of 12 Å. Reciprocal space was sampled using $6 \times 6 \times 1$ mesh. A ferromagnetic spin configuration was initialized for Mn and Ni atoms in the thin film. Structures were relaxed until forces converged below 0.01 eV/Å.

Scanning transmission electron microscopy (STEM): Electron transparent cross-sectional samples for transmission electron microscopy were prepared by means of a FEI Helios NanoLab 600i focused ion beam operated at accelerating voltages of 30 and 5 kV. High-angle annular dark-field scanning transmission electron microscopy (HAADF-STEM), energy dispersive x-ray (EDX) spectroscopy and electron energy-loss spectroscopy (EELS) were carried out using a probe-corrected FEI Titan Themis microscope equipped with ChemiSTEM technology and a CEOS Energy-Filtering and Imaging Device (CEFID) in combination with a direct electron detector (ELA, Dectris Ltd.). The microscope was operated at an accelerating voltage of 300 kV. For the HAADF and EDX data acquisition, a probe convergence semiangle of 18 mrad was set and the annular semidetection range of the annular dark-field detector was calibrated at 84–200 mrad. The elemental maps were calculated from the EDX spectrum image using the Sr K$_\alpha$, Ti K$_\alpha$, La L$_\alpha$, Mn K$_\alpha$ and Ni K$_\alpha$ lines. Note that even though the

EDX spectrum image in Figure 3b was performed with a low beam current of 80 pA, the two top most $Ni_{0.5}Mn_{0.5}O_2$ layers were sputtered away during the 6.6 min long acquisition.

The EELS data were obtained by setting the convergence and collection semiangles to 26 and 35 mrad, respectively, yielding an effective collection semiangle of about 29.5 mrad for the used energy-loss range. An energy dispersion of 0.19 eV/channel was chosen to simultaneously record both the O K and Mn $L_{3,2}$ edges. A 390 x 150 pixel EEL spectrum image (see Figure S6) was acquired with a pixel dwell time of 0.5 ms, resulting in a total acquisition time of 30 s. Note that the electron probe was focused on the film for only about half of the time, while the rest of the time it was focused on the substrate. The low beam current used (80 pA) in combination with the extremely short acquisition time prevented film damage from electron beam irradiation. This was possible thanks to the large CEFID entrance aperture used along with the high sensitivity of the ELA detector. All spectra were background subtracted by fitting a decaying power-law function to an energy window just in front of the core-loss edge onsets. The EEL spectra shown in Figure 3c were calculated by summing all the spectra at each individual $Mn_{0.5}Ni_{0.5}O_2$ slab. The local Mn valence state of each $Mn_{0.5}Ni_{0.5}O_2$ layer is quantified from the Mn $L_{3,2}$ white-line intensity ratio after background subtraction using scaled Hartree-Slater cross-sections.[33,50,51] For the determination of the Mn oxidation state, reference spectra for Mn^{4+} and Mn^{3+} were acquired from $CaMnO_3$ and $YMnO_3$, respectively. The valence state of the manganese atoms is estimated by fitting a linear regression to the experimental Mn L_3/L_2 intensity ratio of the two reference spectra over the manganese valence state. The linear regression produced the following equation: y = 3.85 − 0.47x (where x is the manganese valence state and y is the Mn L_3/L_2 ratio).

WILEY-VCH

Supporting Information

Supporting Information is available from the Wiley Online Library or from the corresponding authors.

Conflict of interest

The authors declare no conflict of interest.

Data availability statement

21

The data that support the findings of this study are available from the corresponding authors upon reasonable request.

Author Contributions

G.D.L. and M.G. conceived the project and designed the experiments. G.D.L., J.S., and S.J. grew and characterized the heterostructures and performed SQUID magnetometry, XAS and XMCD measurements. Synchrotron measurements were supported by A.Z. and C.P. at SLS and C.G. and J.H. at ALBA and were analyzed by G.D.L. TEM specimens were prepared and characterized by M.C., R.E. and M.D.R. DFT calculations were performed by M.K. under the supervision of U.A. First draft of the manuscript was written by G.D.L. and M.G. All authors analyzed the data, discussed the results and contributed to the final version of the paper.

References

[1]   A. Ohtomo, H. Y. Hwang, *Nature* **2004**, *427*, 423.

[2]   A. J. Grutter, H. Yang, B. J. Kirby, M. R. Fitzsimmons, J. A. Aguiar, N. D. Browning, C. A. Jenkins, E. Arenholz, V. V. Mehta, U. S. Alaan, Y. Suzuki, *Phys. Rev. Lett.* **2013**, *111*, 1.

[3]   M. Gibert, P. Zubko, R. Scherwitzl, J. Íñiguez, J.-M. Triscone, *Nat. Mater.* **2012**, *11*, 195.

[4]   J. Chakhalian, J. W. Freeland, H.-U. Habermeier, G. Cristiani, G. Khaliullin, M. van Veenendaal, B. Keimer, *Science (80-.).* **2007**, *318*, 1114.

[5]   A. S. Disa, D. P. Kumah, A. Malashevich, H. Chen, D. A. Arena, E. D. Specht, S. Ismail-Beigi, F. J. Walker, C. H. Ahn, *Phys. Rev. Lett.* **2015**, *114*, 1.

[6]   Z. Zhong, P. Hansmann, *Phys. Rev. X* **2017**, *7*, 011023.

[7]   H. Yamada, Y. Ogawa, Y. Ishii, H. Sato, M. Kawasaki, H. Akoh, Y. Tokura, *Science (80-.).* **2004**, *305*, 646.

[8]   M. Nord, P. E. Vullum, M. Moreau, J. E. Boschker, S. M. Selbach, R. Holmestad, T. Tybell, *Appl. Phys. Lett.* **2015**, *106*, 0.

[9]   H. Boschker, J. Verbeeck, R. Egoavil, S. Bals, G. van Tendeloo, M. Huijben, E. P. Houwman, G. Koster, D. H. A. a Blank, G. Rijnders, *Adv. Funct. Mater.* **2012**, *22*, 2235.

[10]   D. Kan, R. Aso, R. Sato, M. Haruta, H. Kurata, Y. Shimakawa, *Nat. Mater.* **2016**, *15*, 432.

[11]   Z. Liao, M. Huijben, Z. Zhong, N. Gauquelin, S. Macke, R. J. Green, S. Van Aert, J. Verbeeck, G. Van Tendeloo, K. Held, G. A. Sawatzky, G. Koster, G. Rijnders, *Nat. Mater.* **2016**, *15*, 425.

[12]   A. D. Caviglia, S. Gariglio, N. Reyren, D. Jaccard, T. Schneider, M. Gabay, S. Thiel, G. Hammerl, J. Mannhart, J.-M. Triscone, *Nature* **2008**, *456*, 624.

[13]   P. Noël, F. Trier, L. M. Vicente Arche, J. Bréhin, D. C. Vaz, V. Garcia, S. Fusil, A. Barthélémy, L. Vila, M. Bibes, J. P. Attané, *Nature* **2020**, *580*, 483.

[14]   S. Wang, Y. Bai, L. Xie, C. Li, J. D. Key, D. Wu, P. Wang, X. Pan, *ACS Appl. Mater. Interfaces* **2018**, *10*, 1374.

[15]   M. J. Chen, X. K. Ning, Z. J. Wang, P. Liu, S. F. Wang, J. L. Wang, G. S. Fu, S. Ma, W. Liu, Z. D. Zhang, *Appl. Phys. Lett.* **2018**, *112*, 021601.

[16]   N. Nakagawa, H. Y. Hwang, D. A. Muller, *Nat. Mater.* **2006**, *5*, 204.

[17]   R. I. Dass, J.-Q. Yan, J. B. Goodenough, *Phys. Rev. B* **2003**, *68*, 064415.

[18]   N. S. Rogado, J. Li, A. W. Sleight, M. A. Subramanian, *Adv. Mater.* **2005**, *17*, 2225.

[19]   G. De Luca, J. Spring, U. Bashir, M. Campanini, R. Totani, C. Dominguez, A. Zakharova, M. Döbeli, T. Greber, M. D. Rossell, C. Piamonteze, M. Gibert, *APL Mater.* **2021**, *9*, 081111.

[20]   M. C. Sánchez, J. García, J. Blasco, G. Subías, J. Perez-Cacho, *Phys. Rev. B* **2002**, *65*, 144409.

[21]   U. Aschauer, R. Pfenninger, S. M. Selbach, T. Grande, N. A. Spaldin, *Phys. Rev. B* **2013**, *88*, 054111.

[22]   B. Gilbert, B. H. Frazer, A. Belz, P. G. Conrad, K. H. Nealson, D. Haskel, J. C. Lang, G. Srajer, G. De Stasio, *J. Phys. Chem. A* **2003**, *107*, 2839.

[23]   H. Wang, D. S. Patil, W. Gu, L. Jacquamet, S. Friedrich, T. Funk, S. P. Cramer, *J. Electron Spectros. Relat. Phenomena* **2001**, *114–116*, 855.

[24]   X. R. Wang, C. J. Li, W. M. Lu, T. R. Paudel, D. P. Leusink, M. Hoek, N. Poccia, A. Vailionis, T. Venkatesan, J. M. D. Coey, E. Y. Tsymbal, Ariando, H. Hilgenkamp, *Science (80-.).* **2015**, *349*, 716.

[25]   Z. Chen, Z. Chen, Z. Q. Liu, M. E. Holtz, C. J. Li, X. R. Wang, W. M. Lü, M. Motapothula, L. S. Fan, J. A. Turcaud, L. R. Dedon, C. Frederick, R. J. Xu, R. Gao, A. T. N'Diaye, E. Arenholz, J. A. Mundy, T. Venkatesan, D. A. Muller, L.-W. Wang, J. Liu, L. W. Martin, *Phys. Rev. Lett.* **2017**, *119*, 156801.

[26]   L. Yu, A. Zunger, *Nat. Commun.* **2014**, *5*, 5118.

[27]   N. C. Bristowe, P. B. Littlewood, E. Artacho, *Phys. Rev. B* **2011**, *83*, 205405.

[28]   Z. Huang, K. Han, S. Zeng, M. Motapothula, A. Y. Borisevich, S. Ghosh, W. Lü, C. Li, W. Zhou, Z. Liu, M. Coey, T. Venkatesan, Ariando, *Nano Lett.* **2016**, *16*, 2307.

[29]   Z. Wang, A. H. Tavabi, L. Jin, J. Rusz, D. Tyutyunnikov, H. Jiang, Y. Moritomo, J. Mayer, R. E. Dunin-Borkowski, R. Yu, J. Zhu, X. Zhong, *Nat. Mater.* **2018**, *17*, 221.

[30]   S. A. Chambers, L. Qiao, T. C. Droubay, T. C. Kaspar, B. W. Arey, P. V. Sushko, *Phys. Rev. Lett.* **2011**, *107*, 4.

[31]   J. A. Mundy, Y. Hikita, T. Hidaka, T. Yajima, T. Higuchi, H. Y. Hwang, D. A. Muller, L. F. Kourkoutis, *Nat. Commun.* **2014**, *5*, 3464.

[32]   T. C. Kaspar, P. V. Sushko, S. R. Spurgeon, M. E. Bowden, D. J. Keavney, R. B. Comes, S. Saremi, L. Martin, S. A. Chambers, *Adv. Mater. Interfaces* **2019**, *6*, 1.

[33]   M. Varela, M. P. Oxley, W. Luo, J. Tao, M. Watanabe, A. R. Lupini, S. T. Pantelides, S. J. Pennycook, *Phys. Rev. B* **2009**, *79*, 085117.

[34]   P. Agrawal, J. Guo, P. Yu, C. Hébert, D. Passerone, R. Erni, M. D. Rossell, *Phys. Rev. B* **2016**, *94*, 1.

[35]   M. P. Singh, K. D. Truong, S. Jandl, P. Fournier, *J. Appl. Phys.* **2010**, *107*, 09D917.

[36]   S. Catalano, M. Gibert, J. Fowlie, J. Íñiguez, J.-M. Triscone, J. Kreisel, *Reports Prog. Phys.* **2018**, *81*, 046501.

[37]   H. Chen, A. J. Millis, C. A. Marianetti, *Phys. Rev. Lett.* **2013**, *111*, 116403.

[38]   C. Piamonteze, M. Gibert, J. Heidler, J. Dreiser, S. Rusponi, H. Brune, J.-M. M. Triscone, F. Nolting, U. Staub, *Phys. Rev. B* **2015**, *92*, 014426.

[39]   R. Zhang, R. F. Willis, *Phys. Rev. Lett.* **2001**, *86*, 2665.

[40]   L. Wu, C. Li, M. Chen, Y. Zhang, K. Han, S. Zeng, X. Liu, J. Ma, C. Liu, J. Chen, J. Zhang, Ariando, T. V. Venkatesan, S. J. Pennycook, J. M. D. Coey, L. Shen, J. Ma, X. R. Wang, C. W. Nan, *ACS Appl. Mater. Interfaces* **2017**, *9*, 44931.

[41]   G. J. Omar, M. Li, X. Chi, Z. Huang, Z. S. Lim, S. Prakash, S. Zeng, C. Li, X. Yu, C. Tang, D. Song, A. Rusydi, T. Venkatesan, S. J. Pennycook, A. Ariando, *Nano Lett.* **2020**, *20*, 2493.

[42]   C. Lichtensteiger, *J. Appl. Crystallogr.* **2018**, *51*, 1745.

[43]   C. Piamonteze, U. Flechsig, S. Rusponi, J. Dreiser, J. Heidler, M. Schmidt, R. Wetter, M. Calvi, T. Schmidt, H. Pruchova, J. Krempasky, C. Quitmann, H. Brune, F. Nolting, *J. Synchrotron Radiat.* **2012**, *19*, 661.

[44]   A. Barla, J. Nicolás, D. Cocco, S. M. Valvidares, J. Herrero-Martín, P. Gargiani, J. Moldes, C. Ruget, E. Pellegrin, S. Ferrer, *J. Synchrotron Radiat.* **2016**, *23*, 1507.

[45] D. Li, K. Lee, B. Y. Wang, M. Osada, S. Crossley, H. R. Lee, Y. Cui, Y. Hikita, H. Y. Hwang, *Nature* **2019**, *572*, 624.

[46] F. M. F. de Groot, *J. Electron Spectros. Relat. Phenomena* **1994**, *67*, 529.

[47] G. Kresse, *J. Non. Cryst. Solids* **1995**, *192–193*, 222.

[48] P. E. Blöchl, *Phys. Rev. B* **1994**, *50*, 17953.

[49] S. L. Dudarev, G. A. Botton, S. Y. Savrasov, C. J. Humphreys, A. P. Sutton, *Phys. Rev. B* **1998**, *57*, 1505.

[50] T. Riedl, T. Gemming, K. Wetzig, *Ultramicroscopy* **2006**, *106*, 284.

[51] H. K. Schmid, W. Mader, *Micron* **2006**, *37*, 426.

A polar discontinuity at the interface between ferromagnetic insulating double-perovskite La_2NiMnO_6 (LNMO) and $SrTiO_3$ triggers the formation of Mn^{3+} at both LNMO interfaces. Such electron doping is detrimental to Ni/Mn ordering and Curie temperature of films thinner than 10 uc. Engineering the charge transfer with a $LaNiO_3$ overlayer results in optimized ferromagnetic properties, only restricted by dimensionality effects.